Pergamon

Int. J. Heat Mass Transfer. Vol. 39, No. 5, pp. 1067–1080, 1996

0017-9310/96 $15.00+0.00

0017-9310(95)00188-3

Conjugate free convection due to a heated vertical plate

M. VYNNYCKY and S. KIMURA

Tohoku National Industrial Research Institute, Agency of Industrial Science and Technology,
Ministry of International Trade and Industry, Nigatake, 4-2-1, Miyagino-Ku, Sendai 983,
Japan

(*Received* 2 *December* 1994 *and in final form* 21 *April* 1995)

Abstract—Two-dimensional conjugate free convection due to a vertical plate of finite extent adjacent to a semi-infinite fluid region is investigated analytically and numerically. Computed solutions to the governing heat and momentum equations are obtained for a wide range of values of the non-dimensional parameters that are present in the problem, namely the Rayleigh number, *Ra*, the Prandtl number, *Pr*, the thermal conductivity ratio, *k*, between the plate and the fluid medium, and the plate aspect ratio, λ. For $Ra \gg 1$, the results give good agreement with an alternative formulation in which two-dimensional conduction in the solid is coupled with a convective boundary-layer flow in the fluid, the resulting non-linear system of equations then being solved iteratively. In addition, a third, much simpler, approach which assumes one-dimensional conduction in the plate produces accurate easily-obtained formulae for the average conjugate boundary temperature and Nusselt number.

1. INTRODUCTION

Free convective heat transfer arises in many problems of practical engineering interest, for example, in the design of thermal insulation, material processing and geothermal systems; in particular, it has been ascertained that natural convection can induce the thermal stresses which lead to critical structural damage in the piping systems of nuclear reactors [1]. In these situations, overall heat flow depends strongly on the coupling of the boundary conditions between two adjacent media; this is termed a conjugate problem. One case which has received much attention in the past has been that of the two-dimensional free convective flow of a Newtonian fluid heated by a vertical conducting plate of finite thickness, since conduction in the plate is able to affect significantly the natural convection flow over the plate, in particular the heat transfer characteristics. Following early work by Kelleher and Yang [2], Ziness [3], Chida and Katto [4] and Gdalevich and Fertman [5], Miyamoto *et al.* [6] provided both experimental results and an approximate solution valid for a boundary-layer regime. Miyamoto and Nishiyama [7] and Miyamoto and Sumikawa [8] have provided computed solutions to the governing equations when the conducting plate is of infinite length. Subsequently, Timma and Padet [9] and Pozzi and Lupo [10] have made analytical progress by assuming a thin heated plate so that conduction within the solid is one-dimensional. Merkin and Pop [11] have indicated that this procedure leaves only the Prandtl number as a relevant dimensionless parameter in the problem and have furthermore provided a numerical solution to the boundary-layer equations for this case.

In view of the above, conjugate heat transfer for the most general case, when the heated vertical plate is assumed to be of both finite thickness and length, corresponding to the presence of axial conduction effects, has yet to be treated fully; in particular, the singularity present at the leading edge of the plate, suggested by Miyamoto *et al.* [6] remains unresolved. These issues, therefore, form the purpose of the present paper. First, we provide a mathematical formulation for the full problem, identifying the relevant nondimensional parameters to be, in addition to the Rayleigh number (*Ra*) and the Prandtl number (*Pr*), the thermal conductivity ratio, *k*, between the solid and the fluid, and the plate aspect ratio, λ. The high Rayleigh number regime is treated in two ways: first, by coupling the boundary-layer flow within the fluid to two-dimensional conduction within the plate, and solving the resultant problem numerically, and second, by averaging over the plate length to obtain the average conjugate boundary temperature and mean Nusselt number. The full equations are then solved numerically by finite-difference techniques using a transformation from Cartesian to elliptic coordinates for the fluid domain; this ensures the clustering of grid points, and thus increased resolution, in the vicinity of greatest interest near the plate. Results obtained using all three methods are presented and compared for a wide range of values of *Ra*, *Pr*, *k* and λ.

2. MATHEMATICAL FORMULATION

Consider the steady free convective flow due to a rectangular plate occupying the region

NOMENCLATURE

a	thickness of the conducting plate
b	length of the conducting plate
g	acceleration due to gravity
k_f	thermal conductivity of the fluid medium
k_s	thermal conductivity of the plate
k	thermal conductivity ratio, k_s/k_f
Nu	dimensionless local Nusselt number
$\bar{Nu}$	dimensionless average Nusselt number
T_c	constant temperature of heated side of plate
T_∞	constant temperature of ambient fluid
Pr	Prandtl number for the fluid, ν/α
Ra	Rayleigh number for the fluid, $g\beta b^3(T_c - T_\infty)/\alpha\nu$
x	horizontal coordinate
y	vertical coordinate
u, v	dimensionless velocity components along (x, y) axes
x_∞	size of computational domain in x-direction
M_x	total number of grid points in x-direction in conducting plate
M_y	total number of grid points in y-direction in conducting plate.

Greek symbols

α	thermal diffusivity
β	coefficient of thermal expansion
ν	kinematic viscosity
λ	aspect ratio, a/b
θ_s	dimensionless temperature in the solid
θ_f	dimensionless temperature in the fluid medium
θ_b	dimensionless boundary temperature
$\bar{\theta}_b$	dimensionless average boundary temperature
ξ_∞	size of computational domain in ξ-direction
ψ	dimensionless streamfunction
ω	dimensionless vorticity
$\Delta\theta$	temperature increment
$\Delta\psi$	streamline increment
M_η	total number of grid points in η-direction in fluid medium
M_ξ	total number of grid points in ξ-direction in fluid medium
ζ	similarity variable.

$$-a \leqslant x \leqslant 0, \quad -\frac{b}{2} \leqslant y \leqslant \frac{b}{2},$$

adjacent to a semi-infinite region of incompressible fluid ($x > 0$, $-\infty < y < \infty$) at temperature T_∞ (Fig. 1). The left-hand side of the plate is held at a uniform temperature $T_c(> T_\infty)$, whilst its horizontal sides at $y = \pm b/2$ are insulated. The boundary at $x = 0$ is taken to be no-slip, with the portion for $|y| > b/2$ insulated, so that heat flows into $x > 0$ only via $|y| < b/2$. Invoking the Boussinesq approximation for the body forces, and using the streamfunction vorticity ($\psi - \omega$) formulation, where the (x, y) components of the velocity field, (u, v), are related to the streamfunction by

$$u = \frac{\partial \psi}{\partial y}, \quad v = -\frac{\partial \psi}{\partial x}$$

and the vorticity is defined by

$$\omega = \frac{\partial v}{\partial x} - \frac{\partial u}{\partial y}$$

free convective flow is described by the streamfunction equation,

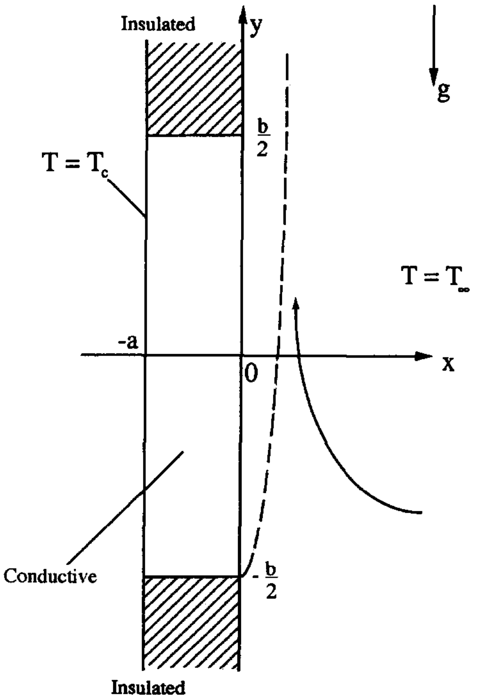

Fig. 1. Sketch of geometry for natural convection.

$$\frac{\partial^2\psi}{\partial x^2}+\frac{\partial^2\psi}{\partial y^2}=-\omega \tag{1}$$

the vorticity transport equation

$$u\frac{\partial\omega}{\partial x}+v\frac{\partial\omega}{\partial y}=\nu\left(\frac{\partial^2\omega}{\partial x^2}+\frac{\partial^2\omega}{\partial y^2}\right)+\boldsymbol{g}\beta\frac{\partial T_f}{\partial x} \tag{2}$$

the equation of energy in the fluid region

$$u\frac{\partial T_f}{\partial x}+v\frac{\partial T_f}{\partial y}=\alpha\left(\frac{\partial^2 T_f}{\partial x^2}+\frac{\partial^2 T_f}{\partial y^2}\right) \tag{3}$$

and the equation of energy in the solid plate

$$\frac{\partial^2 T_s}{\partial x^2}+\frac{\partial^2 T_s}{\partial y^2}=0. \tag{4}$$

Here, T_f and T_s are the temperatures of the fluid and the solid plate, respectively, and the physical constants $\boldsymbol{g}$, β, ν, α (and later k_s and k_f) are as given in the Nomenclature. Equations (1)–(4) are subject to the following boundary conditions:

$$\psi=\frac{\partial\psi}{\partial x}=0 \quad \text{on} \quad x=0, \tag{5}$$

$$T_s=T_f,\quad k_f\frac{\partial T_f}{\partial x}=k_s\frac{\partial T_s}{\partial x}, \quad \text{on} \quad x=0,\quad |y|\leqslant\frac{b}{2} \tag{6}$$

$$\frac{\partial T_f}{\partial x}=0 \quad \text{on} \quad x=0,\quad |y|>\frac{b}{2} \tag{7}$$

$$T_s=T_c \quad \text{on} \quad x=-a,\quad |y|\leqslant\frac{b}{2} \tag{8}$$

$$\frac{\partial T_s}{\partial y}=0 \quad \text{on} \quad y=\pm\frac{b}{2},\quad -a\leqslant x\leqslant 0. \tag{9}$$

The outer boundary conditions must be treated in two parts: one with fluid coming into the solution domain at ambient temperature (inflow boundary condition),

$$\begin{gathered}v\to 0,\quad \frac{\partial^2\psi}{\partial x^2}\to 0,\quad T_f\to T_\infty,\quad \omega\to-\frac{\partial^2\psi}{\partial y^2} \quad \text{as } x\to\infty\\ u\to 0,\quad \frac{\partial^2\psi}{\partial y^2}\to 0,\quad T_f\to T_\infty,\quad \omega\to-\frac{\partial^2\psi}{\partial x^2} \quad \text{as } y\to\pm\infty\end{gathered} \tag{10}$$

the other with fluid leaving the solution domain with negligible normal temperature gradient (outflow boundary condition),

$$\begin{gathered}v\to 0,\quad \frac{\partial^2\psi}{\partial x^2}\to 0,\quad \frac{\partial T_f}{\partial x}\to 0,\quad \omega\to-\frac{\partial^2\psi}{\partial y^2} \quad \text{as } x\to\infty\\ u\to 0,\quad \frac{\partial^2\psi}{\partial y^2}\to 0,\quad \frac{\partial T_f}{\partial y}\to 0,\quad \omega\to-\frac{\partial^2\psi}{\partial x^2} \quad \text{as } y\to\pm\infty.\end{gathered}$$

By employing the following nondimensionalization,

$$x^*=\frac{x}{b},\quad y^*=\frac{y}{b},\quad u^*=\frac{bu}{\alpha}$$

$$v^*=\frac{bv}{\alpha},\quad \psi^*=\frac{\psi}{\alpha},\quad \omega^*=\frac{\omega b^2}{\alpha}$$

$$\theta_s^*=\frac{T_s-T_\infty}{T_c-T_\infty},\quad \theta_f^*=\frac{T_f-T_\infty}{T_c-T_\infty} \tag{12}$$

and subsequently, dropping the asterisks, we arrive at the following system of dimensionless equations for the fluid region

$$\nabla^2\psi=-\omega \tag{13}$$

$$\frac{1}{Pr}\left(u\frac{\partial\omega}{\partial x}+v\frac{\partial\omega}{\partial y}\right)=\nabla^2\omega+Ra\frac{\partial\theta_f}{\partial x} \tag{14}$$

$$u\frac{\partial\theta_f}{\partial x}+v\frac{\partial\theta_f}{\partial y}=\nabla^2\theta_f \tag{15}$$

where $Ra=\boldsymbol{g}\beta b^3(T_c-T_\infty)/\alpha\nu$ is the Rayleigh number, $Pr=\nu/\alpha$ is the Prandtl number and ∇^2 denotes the two-dimensional Laplacian operator; in addition, conductive heat transfer in the solid is given by

$$\nabla^2\theta_s=0 \tag{16}$$

where θ_s denotes the dimensionless temperature. Equations (13)–(16) are now subject to the non-dimensional form of the boundary conditions (5)–(11), that is

$$\psi=\frac{\partial\psi}{\partial x}=0 \quad \text{on} \quad x=0, \tag{17}$$

$$\theta_s=\theta_f,\quad \frac{\partial\theta_f}{\partial x}=k\frac{\partial\theta_s}{\partial x} \quad \text{on} \quad x=0,\quad |y|\leqslant\tfrac{1}{2} \tag{18}$$

$$\frac{\partial\theta_f}{\partial x}=0 \quad \text{on} \quad x=0,\quad |y|>\tfrac{1}{2} \tag{19}$$

$$\theta_s=1 \quad \text{on} \quad x=-\lambda,\quad |y|\leqslant\tfrac{1}{2} \tag{20}$$

$$\frac{\partial\theta_s}{\partial y}=0 \quad \text{on} \quad y=\pm\tfrac{1}{2},\quad -\lambda<x\leqslant 0 \tag{21}$$

with inflow and outflow conditions as

$$\begin{gathered}v\to 0,\quad \frac{\partial^2\psi}{\partial x^2}\to 0,\quad \theta_f\to 0,\quad \omega\to-\frac{\partial^2\psi}{\partial y^2} \quad \text{as} \quad x\to\infty\\ u\to 0,\quad \frac{\partial^2\psi}{\partial y^2}\to 0,\quad \theta_f\to 0,\quad \omega\to-\frac{\partial^2\psi}{\partial x^2} \quad \text{as} \quad y\to\pm\infty\end{gathered} \tag{22}$$

and

$$\begin{gathered}v\to 0,\quad \frac{\partial^2\psi}{\partial x^2}\to 0\\ \frac{\partial\theta_f}{\partial x}\to 0,\quad \omega\to-\frac{\partial^2\psi}{\partial y^2} \quad \text{as} \quad x\to\infty\\ u\to 0,\quad \frac{\partial^2\psi}{\partial y^2}\to 0\\ \frac{\partial\theta_f}{\partial y}\to 0,\quad \omega\to-\frac{\partial^2\psi}{\partial x^2} \quad \text{as} \quad y\to\pm\infty,\end{gathered} \tag{23}$$

respectively. In equations (13)–(23), $\lambda = a/b$ denotes the aspect ratio of the the conducting plate and $k = k_s/k_f$ is the ratio of the thermal conductivities in the conducting solid and the fluid medium.

In this formulation, the heat transfer rate is expressed in terms of the local and mean Nusselt numbers given by

$$Nu = -\left(\frac{\partial \theta_f}{\partial x}\right)_{x=0} \quad |y| \leqslant \tfrac{1}{2} \tag{24}$$

and

$$\bar{Nu} = \int_{-1/2}^{1/2} Nu \, dy. \tag{25}$$

3. THEORETICAL CONSIDERATIONS FOR *Ra* ≫ 1

3.1. *Formulation*

We attempt first a solution for the case $Ra \gg 1$. This assumes that, at the conjugate boundary, there are thermal and viscous boundary layers whose convective heat flow is coupled to the conductive heat flow within the solid. Denoting by θ_0 the temperature at $(0, -\frac{1}{2})$, where it is evident that $0 \leqslant \theta_0 \leqslant 1$, two cases emerge. We consider first $\theta_0 > 0$, and turn to the $\theta_0 = 0$ case later.

For $\theta_0 > 0$, the boundary layer locally is temperature-driven, so that the appropriate rescalings when $Pr \sim O(1)$ are given by

$$\psi = Ra^{1/4}\Psi \quad \omega = Ra^{3/4}\Omega \quad x = Ra^{-1/4}X \tag{26}$$

so that equations (13)–(15) ultimately reduce, on eliminating Ω, to

$$\frac{1}{Pr}\left(\frac{\partial \Psi}{\partial X}\frac{\partial^2 \Psi}{\partial X \partial Y} - \frac{\partial \Psi}{\partial Y}\frac{\partial^2 \Psi}{\partial X^2}\right) = -\frac{\partial^3 \Psi}{\partial X^3} + \theta_f \tag{27}$$

$$\frac{\partial \Psi}{\partial Y}\frac{\partial \theta_f}{\partial X} - \frac{\partial \Psi}{\partial X}\frac{\partial \theta_f}{\partial Y} = \frac{\partial^2 \theta_f}{\partial X^2} \tag{28}$$

with $Y = y + \frac{1}{2}$, so that the start of the boundary layer is shifted to the origin. The boundary conditions relevant to the layer are now

$$\Psi = \frac{\partial \Psi}{\partial X} = 0 \quad \text{on} \quad X = 0, \tag{29}$$

$$\theta_s = \theta_f \quad \text{on} \quad X = 0, \quad 0 \leqslant Y \leqslant 1 \tag{30}$$

$$\frac{\partial \theta_s}{\partial x} = \sigma \frac{\partial \theta_f}{\partial X} \quad \text{on} \quad X = 0, \quad 0 \leqslant Y \leqslant 1 \tag{31}$$

$$\frac{\partial^2 \Psi}{\partial X^2} \to 0, \quad \theta_f \to 0, \quad \Omega \to 0 \quad \text{as} \quad X \to \infty \tag{32}$$

where we have identified $\sigma = Ra^{1/4}k^{-1}$ as a dimensionless parameter. Boundary conditions are also required at $Y = 0$. These come from assuming that the flow is stagnant for $Y \leqslant 0$, so that the appropriate conditions are

$$\Psi = \frac{\partial \Psi}{\partial Y} = 0 \quad \text{at} \quad Y = 0 \tag{33}$$

we return to the validity of this assumption in Section 5.

For the purpose of analytical development and ultimate numerical solution, it is better to reformulate equations (27)–(33) using similarity-like variables. Writing

$$\Psi(X, Y) = Y^{3/4}F(\zeta, Y)$$
$$\theta_f(X, Y) = G(\zeta, Y), \quad \zeta = \frac{X}{Y^{1/4}} \tag{34}$$

equations (27) and (28) reduce to

$$F''' + \frac{1}{Pr}\left(\tfrac{1}{2}F'^2 - \tfrac{3}{4}FF''\right) - G = \frac{Y}{Pr}\left(F''\frac{\partial F}{\partial Y} - F'\frac{\partial F'}{\partial Y}\right) \tag{35}$$

$$G'' - \tfrac{3}{4}FG' = Y\left(G'\frac{\partial F}{\partial Y} - F'\frac{\partial G'}{\partial Y}\right) \tag{36}$$

where the primes denote differentiation with respect to ζ. The boundary conditions for $0 \leqslant Y \leqslant 1$ in terms of F and G are

$$F = F' = 0 \quad \text{on} \quad \zeta = 0 \tag{37}$$

$$\theta_s = G \quad \text{on} \quad \zeta = 0 \tag{38}$$

$$\frac{\partial \theta_s}{\partial x} = \frac{\sigma}{Y^{1/4}}G' \quad \text{on} \quad \zeta = 0 \tag{39}$$

$$F' \to 0, \quad G \to 0 \quad \text{as} \quad \zeta \to \infty \tag{40}$$

with equation (33) satisfied automatically by the choice of variables. Letting $Y \to 0$, we arrive at the ordinary differential equations

$$F''' + \frac{1}{Pr}\left(\tfrac{1}{2}F'^2 - \tfrac{3}{4}FF''\right) - G = 0 \tag{41}$$

$$G'' - \tfrac{3}{4}FG' = 0 \tag{42}$$

subject to

$$F = F' = 0 \quad \text{on} \quad \zeta = 0, \tag{43}$$

$$F' \to 0, \quad G \to 0 \quad \text{as} \quad \zeta \to \infty \tag{44}$$

but with equation (38) now replaced by

$$G = \theta_0 \quad \text{on} \quad \zeta = 0 \tag{45}$$

where the constant θ_0 is, of course, as yet unknown. Furthermore, the canonical substitution

$$G = \theta_0 \hat{G} \quad \zeta = \theta_0^{-1/4}\hat{\zeta} \quad F = \theta_0^{1/4}\hat{F} \tag{46}$$

removes θ_0 from the system of equations (41)–(44), which may be solved once and for all ahead of the rest of the computations.

Next, we observe that the condition for continuity of heat flux at the conjugate boundary in the vicinity of $Y = 0$ has become

$$\frac{\partial \theta_s}{\partial x} = \frac{\sigma \theta_0^{5/4}}{Y^{1/4}}\hat{G}'(0). \tag{47}$$

Introducing plane polar coordinates (r, ϕ), given by

$$x = r\cos\phi, \quad Y = r\sin\phi$$

we note that boundary conditions (21) and (47) become

$$\frac{\partial\theta_s}{\partial\phi} = 0 \quad \text{on} \quad \phi = \pi \tag{48}$$

$$\frac{\partial\theta_s}{\partial\phi} = -\frac{Ra^{1/4}\theta_0^{5/4}\hat{G}'(0)}{k} r^{3/4} \quad \text{on} \quad \phi = \frac{\pi}{2}. \tag{49}$$

A solution of equation (16) which satisfies these boundary conditions is

$$\hat{\theta}_s(r,\phi) = \frac{4\sigma\theta_0^{5/4}\hat{G}'(0)}{3\sin\frac{3\pi}{8}} r^{3/4}\cos\tfrac{3}{4}(\phi-\pi) \tag{50}$$

so that we may remove the singularity at $r = 0$ by writing $\theta_s = \hat{\theta}_s + \theta_s^*$. Thence, θ_s^* satisfies

$$\nabla^2\theta_s^* = 0 \tag{51}$$

subject to

$$\theta_s^* = \theta_0\hat{G} - \hat{\theta}_s \quad \text{on} \quad x = 0, \quad 0 \leqslant Y \leqslant 1 \tag{52}$$

$$\frac{\partial\theta_s^*}{\partial x} = \frac{\sigma\theta_0^{5/4}}{Y^{1/4}}\hat{G}' - \frac{\partial\hat{\theta}_s}{\partial x} \quad \text{on} \quad x = 0, \quad 0 \leqslant Y \leqslant 1 \tag{53}$$

$$\frac{\partial\theta_s^*}{\partial Y} = 0 \quad \text{on} \quad Y = 0, \quad -\lambda \leqslant x \leqslant 0 \tag{54}$$

$$\frac{\partial\theta_s^*}{\partial Y} = -\frac{\partial\hat{\theta}_s}{\partial Y} \quad \text{on} \quad Y = 1, \quad -\lambda \leqslant x \leqslant 0 \tag{55}$$

$$\theta_s^* = 1 - \hat{\theta}_s \quad \text{on} \quad x = -\lambda, \quad 0 \leqslant Y \leqslant 1. \tag{56}$$

Recast into this form, with the singularity at $r = 0$ removed, the equations are amenable to numerical solution by methods to be described shortly, provided $\theta_0 > 0$. The case when $\theta_0 = 0$ proceeds slightly differently, however, and we include it for completeness.

This case is accommodated by choosing the similarity-like variables to be

$$\Psi(X, Y) = Y^{4/5}F(\zeta, Y)$$

$$\theta_f(X, Y) = Y^{1/5}G(\zeta, Y), \quad \zeta = \frac{X}{Y^{1/5}}. \tag{57}$$

Equations (27) and (28) now become

$$F''' + \frac{1}{Pr}(\tfrac{3}{5}F'^2 - \tfrac{4}{5}FF'') - G = \frac{Y}{Pr}\left(F''\frac{\partial F}{\partial Y} - F'\frac{\partial F'}{\partial Y}\right) \tag{58}$$

$$G'' - \tfrac{4}{5}FG' + \tfrac{1}{5}F'G = Y\left(G'\frac{\partial F}{\partial Y} - F'\frac{\partial G'}{\partial Y}\right). \tag{59}$$

The boundary conditions in terms of F and G this time are

$$F = F' = 0 \quad \text{on} \quad \zeta = 0 \tag{60}$$

$$\theta_s = Y^{1/5}G \quad \text{on} \quad \zeta = 0 \tag{61}$$

$$\frac{\partial\theta_s}{\partial x} = \sigma G' \quad \text{on} \quad \zeta = 0 \tag{62}$$

$$F' \to 0 \quad G \to 0 \quad \text{as} \quad \zeta \to \infty \tag{63}$$

with equation (33) satisfied automatically by the choice of variables. Letting $Y \to 0$, we arrive at

$$F''' + \frac{1}{Pr}(\tfrac{3}{5}F'^2 - \tfrac{4}{5}FF'') - G = 0 \tag{64}$$

$$G'' - \tfrac{4}{5}FG' + \tfrac{1}{5}F'G = 0 \tag{65}$$

subject to

$$F = F' = 0 \quad \text{on} \quad \zeta = 0 \tag{66}$$

$$F' \to 0 \quad G \to 0 \quad \text{as} \quad \zeta \to \infty \tag{67}$$

but with equation (38) now automatically satisfied, thanks to the choice of similarity-like variables. The seeming shortfall in boundary conditions is remedied by observing that the canonical forms

$$G = Q^{4/5}\hat{G} \quad \zeta = Q^{-1/5}\hat{\zeta} \quad F = Q^{1/5}\hat{F}$$

are also solutions to equations (64)–(67), with Q a constant to be determined. Subsequently, $\hat{F}$ and $\hat{G}$ satisfy equations (64)–(67), with the extra boundary condition appearing in the form

$$\hat{G}'(0) = -1 \tag{68}$$

and with Q being determined from the continuity of heat flux at $Y = 0$ once the solution for θ_s has been found. This time, there is no singularity near the origin with respect to θ_s, which now satisfies the boundary conditions

$$\theta_s = Q^{4/5}Y^{1/5}\hat{G} \quad \text{on} \quad x = 0, \quad 0 < Y < 1 \tag{69}$$

$$\frac{\partial\theta_s}{\partial x} = Q\sigma\hat{G}' \quad \text{on} \quad x = 0, \quad 0 < Y < 1 \tag{70}$$

$$\theta_s = 1 \quad \text{on} \quad x = -\lambda, \quad 0 < Y < 1 \tag{71}$$

$$\frac{\partial\theta_s}{\partial Y} = 0 \quad \text{on} \quad Y = 0, 1, \quad -\lambda \leqslant x \leqslant 0. \tag{72}$$

3.2. *Solution*

We proceed by indicating the method used for a numerical solution of the above equations.

For the case $\theta_0 > 0$, an initial guess was made for θ_s^* and $\hat{G}'$ at the conjugate boundary (note that $\theta_s^* = \theta_0$). Then, equation (51) was solved subject to equations (53)–(56) using Gauss–Seidel iteration with a 50×50 mesh to produce updated values for θ_s^*. Updating the value of θ_0 at this point, however, was found to lead to non-convergence of the scheme, and therefore an outer loop was required for this purpose. Then, Runge–Kutta and shooting was used to solve the canonical form of equations (41)–(45), and the solution was then used as the initial condition for the boundary–layer integration. For this, equations (35) and (36) were solved using the Keller–Box method

[14], subject to equations (37), (38) and (40); as for the grid, we took the same number of points in the Y-direction as was taken for the solution of equation (51), and 401 points in the ζ-direction, with the outer edge of the boundary layer set at $\zeta_\infty = 15$. This generated an updated set of $\hat{G}'$ values at $\zeta = 0$, to be used in solving again for θ_s^*, and so on. This iterative procedure was repeated until the following convergence criterion was satisfied:

$$\max_{i=1,50} |\theta_s^{(n+1)} - \theta_s^{(n)}| < 10^{-6}$$

with n denoting the iteration order. For the case when $\theta_0 = 0$, the solution procedure was basically similar, although modifications were of course required in the code used for the Keller–Box method.

In the course of solution, several trends regarding the values of the parameters σ, Pr and λ became apparent. Starting with the case $Pr = 1$, $\lambda = 1$, the scheme was found to be rapidly convergent for $\sigma < 1.6$, corresponding to, for $Ra = 10^6$, $k = 20$. For these cases, setting θ_s equal to one along the conjugate boundary was sufficient to provide a converged solution. For σ in excess of 1.6, it proved impossible to obtain converged solutions, even by taking good initial guesses such as converged solutions for lower values of σ. A similar trend was observed for $\lambda = 0.1$, although here the threshold in σ for converged solutions was found to be much higher at around 10.5; the value of Pr, on the other hand, was not observed to have much effect on the σ-threshold value. In summary, therefore, the scheme is found to work well provided that, for Ra greater than $O(10^5)$, k is of $O(1)$; this would appear to be a parameter range suitable in many applications (see, for example, the tables of material properties in Holman [15]).

One further point of relevance in this section is the physical meaning of the case $\theta_0 = 0$. In fact, this is the limiting case when either Ra is infinite or $k = 0$; consequently, solutions obtained for this case only approach a physical meaning if $\sigma \gg 1$, although for finite values of σ, it makes more sense to use the $\theta_0 > 0$ formulation. Thus, the $\theta_0 = 0$ case is taken no further, but results for $\theta_0 > 0$ will be presented in Section 5, along with a numerical solution to the full equations.

3.3. *One-dimensional analogue*

A simpler approach in order to estimate the average conjugate boundary temperature, $\bar{\theta}_b$, and Nusselt number, $\bar{Nu}$, when $Ra \gg 1$ is to assume heat flow to be one-dimensional within the plate, and to consider the plate-averaged, rather than local, Nusselt number due to the boundary-layer flow within the fluid. We consider first the case for $Pr \sim O(1)$ and greater.

Defining, for the purposes of later comparison, $\bar{\theta}_b$ by

$$\bar{\theta}_b = \int_{-1/2}^{1/2} \theta_f(0, y)\, dy$$

we note, using the scalings of equation (26) and the canonical transformation of equation (46) (with θ_0 replaced by $\bar{\theta}_b$), that equation (18), integrated and averaged for $-\frac{1}{2} \leqslant y \leqslant \frac{1}{2}$, reduces to

$$\frac{k}{\lambda}(\bar{\theta}_b - 1) = \tfrac{4}{3} Ra^{1/4} \bar{\theta}_b^{5/4} \hat{G}'(0) \qquad (73)$$

with $\hat{G}'(0)$, which depends only on the Prandtl number, coming from the solution of equations (41)–(44). Noting that $\hat{G}'(0) < 0$ for all values of Pr, we set $\mu = -4\lambda Ra^{1/4} \hat{G}'(0)/3k$ and $Z = \bar{\theta}_b^{1/4}$, so that equation (73) becomes the quintic equation

$$F_\mu(Z) \equiv \mu Z^5 + Z^4 - 1 = 0. \qquad (74)$$

This does not possess a closed form solution, although it is possible to obtain the properties of the solution before finding the roots numerically. First, elementary asymptotic analysis indicates that

$$\bar{\theta}_b \sim 1 - \mu \quad \mu \ll 1, \qquad (75)$$

$$\bar{\theta}_b \sim \mu^{-4/5} \quad \mu \gg 1. \qquad (76)$$

Next, since equation (74) possesses only two turning points (at $Z = 0$ and $-4/5\mu$), it is clear that at most there can be only three real solutions. Furthermore, since $F_\mu(1) = \mu > 0$ and $F_\mu(0) = -1$, we can deduce that exactly one of these must lie in the range $0 \leqslant Z \leqslant 1$. However, in order to demonstrate that this solution is the only physically acceptable one, in the sense that $|\bar{\theta}_b| \leqslant 1$, we require to show that the other two solutions lie in the region $|Z| > 1$. Since $F_\mu(-1) = -\mu < 0$, it is clear that the other two solutions both lie either in the interval $-1 \leqslant Z \leqslant 0$, or in the range $-\infty < Z \leqslant -1$; the latter case implies that there is only one physically acceptable solution as required, so we need only consider the former. In this case, if there is to be more than one solution, we require that the turning point at $Z = -4/5\mu$ lies in $(-1, 0)$ and that $F_\mu(-4/5\mu) \geqslant 0$; the first condition requires that $\mu \geqslant \frac{4}{5}$, whilst the second leads to $\mu \leqslant 4/5^{5/4}$, giving the required contradiction.

In the light of this analysis, the unique solution for $\bar{\theta}_b$ as a function of μ may be found using a straightforward Newton–Raphson technique; the results are plotted in Fig. 2, and will be compared later with the

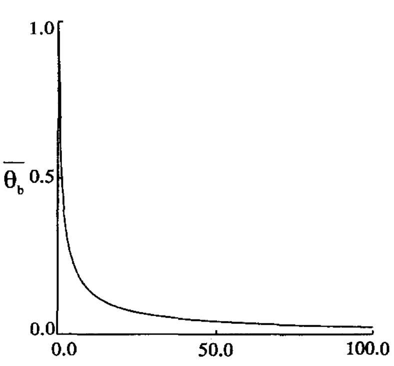

Fig. 2. Solution to equation (74) for $\bar{\theta}_b$ as a function of μ.

numerical computations of Section 5. Note that for $\bar{\theta}_b$, all the results, regardless of the values of Ra, k, λ and Pr, may be collapsed onto one curve, as in Fig. 2: this is not, however, the case for $\bar{N}u$ which is given by

$$\bar{N}u = -\tfrac{4}{3}Ra^{1/4}\hat{G}'(0)\bar{\theta}_b^{5/4}. \tag{77}$$

The case for $Pr \ll 1$, $Ra\,Pr \gg 1$ proceeds in similar fashion, except that scaling (26) is now replaced by

$$\psi = (Ra\,Pr)^{1/4}\Psi, \quad \omega = (Ra\,Pr)^{3/4}\Omega,$$
$$x = (Ra\,Pr)^{-1/4}X. \tag{78}$$

Equations (41)–(44) now become

$$\tfrac{1}{2}F'^2 - \tfrac{3}{4}FF'' - G = 0 \tag{79}$$

$$G'' - \tfrac{3}{4}FG' = 0 \tag{80}$$

subject to

$$F = 0 \quad \text{on} \quad \zeta = 0 \tag{81}$$

$$F' \to 0 \quad G \to 0 \quad \text{as} \quad \zeta \to \infty \tag{82}$$

$$G = \bar{\theta}_b \quad \text{on} \quad \zeta = 0. \tag{83}$$

The same canonical transformation as before gives the standard equations, whose solution produces $\hat{G}'(0)$, now independent of Pr, equal to 0.6. This time we set $\mu = -4\lambda(Ra\,Pr)^{1/4}\hat{G}'(0)/3k$, obtaining $\bar{\theta}_b$ in the same way as before, although with $\bar{N}u$ now given by

$$\bar{N}u = -\tfrac{4}{3}(Ra\,Pr)^{1/4}\hat{G}'(0)\bar{\theta}_b^{5/4}. \tag{84}$$

Despite the approximate nature of this analytical approach, it does nevertheless, from an engineering perspective, provide easily obtainable results for $\bar{\theta}_b$ and $\bar{N}u$ which, it turns out, compare very well with the full computed solutions of the next section.

4. NUMERICAL SOLUTION

For the purposes of computation, the governing equations for the fluid are first recast into elliptic (ξ, η) coordinates, with the advantage that the region near the plate is effectively magnified. These are related to Cartesian coordinates by

$$x = \tfrac{1}{2}\sinh\xi\sin\eta, \quad y = -\tfrac{1}{2}\cosh\xi\cos\eta,$$

so that equations (13)–(15) become

$$\frac{\partial^2\psi}{\partial\xi^2} + \frac{\partial^2\psi}{\partial\eta^2} = -\frac{M^2(\xi,\eta)}{4}\omega \tag{85}$$

$$\frac{1}{Pr}\left(\frac{\partial\psi}{\partial\xi}\frac{\partial\omega}{\partial\eta} - \frac{\partial\psi}{\partial\eta}\frac{\partial\omega}{\partial\xi}\right) = \frac{\partial^2\omega}{\partial\xi^2} + \frac{\partial^2\omega}{\partial\eta^2}$$
$$+\frac{Ra}{2}\left(\cosh\xi\sin\eta\frac{\partial\theta_f}{\partial\xi} + \sinh\xi\cos\eta\frac{\partial\theta_f}{\partial\eta}\right) \tag{86}$$

$$\left(\frac{\partial\psi}{\partial\xi}\frac{\partial\theta_f}{\partial\eta} - \frac{\partial\psi}{\partial\eta}\frac{\partial\theta_f}{\partial\xi}\right) = \frac{\partial^2\theta_f}{\partial\xi^2} + \frac{\partial^2\theta_f}{\partial\eta^2} \tag{87}$$

where $M^2(\xi,\eta) = \frac{1}{2}(\cosh 2\xi - \cos 2\eta)$. Equation (16) is kept in Cartesian coordinates, but the boundary conditions are now,

$$\psi = \frac{\partial\psi}{\partial\xi} = 0 \quad \text{on} \quad \xi = 0 \tag{88}$$

$$\psi = \frac{\partial\psi}{\partial\eta} = 0 \quad \text{on} \quad \eta = 0, \pi \tag{89}$$

$$\theta_s = \theta_f, \quad \frac{2}{k\sin\eta}, \quad \frac{\partial\theta_f}{\partial\xi} = \frac{\partial\theta_s}{\partial x} \quad \text{on} \quad \xi = 0 \tag{90}$$

$$\frac{\partial\theta_f}{\partial\eta} = 0 \quad \text{on} \quad \eta = 0, \pi \tag{91}$$

$$\theta_s = 1 \quad \text{on} \quad x = -\lambda, \quad |y| \leqslant \tfrac{1}{2} \tag{92}$$

$$\frac{\partial\theta_s}{\partial y} = 0 \quad \text{on} \quad y = \pm\tfrac{1}{2}, \quad -\lambda \leqslant x \leqslant 0 \tag{93}$$

furthermore, denoting by (u_η, u_ξ) the velocity components in (η, ξ)-coordinates, which are given in terms of ψ by

$$u_\eta = -\frac{2}{M}\frac{\partial\psi}{\partial\xi}, \quad u_\xi = \frac{2}{M}\frac{\partial\psi}{\partial\eta}$$

the inflow and outflow boundary conditions become

$$u_\eta \to 0, \quad \frac{\partial^2\psi}{\partial\xi^2} \to 0$$
$$\theta_f \to 0, \quad \omega \to -\frac{4}{M^2}\frac{\partial^2\psi}{\partial\eta^2} \quad \text{as} \quad \xi \to \infty \tag{94}$$

and

$$u_\eta \to 0, \quad \frac{\partial^2\psi}{\partial\xi^2} \to 0$$
$$\frac{\partial\theta_f}{\partial\xi} \to 0, \quad \omega \to -\frac{4}{M^2}\frac{\partial^2\psi}{\partial\eta^2} \quad \text{as} \quad \xi \to \infty \tag{95}$$

respectively.

The partial differential equations (86) and (87) were finite-differenced using a control volume approach and non-uniform grid network as described by Patankar [13]; a standard second-order accurate five-point scheme was used for equations (85) and (16). The mesh was refined in the ξ-direction near $\xi = 0$ in order to resolve the boundary layer, of thickness $Ra^{1/4}$, that is present for $Ra \gg 1$; consequently (η, ξ) mesh sizes of 31×40 and 31×80, both containing at least five points in the boundary layer for Ra as high as 10^6, were used for validating the code. For the solid, a non-uniform 20×31 mesh, with the same number of mesh points for y as for η, was used; refinement in the x-direction was also used in order to take adequate account of equation (90). The inflow/outflow conditions were treated by first amalgamating into the form

$$u_\eta = 0, \quad \omega = -\frac{4}{M^2}\frac{\partial^2\psi}{\partial\eta^2} \quad \text{at} \quad \xi = \xi_\infty$$

$$\theta_f = 0 \quad \text{if} \quad u_\xi < 0 \quad \text{at} \quad \xi = \xi_\infty$$

$$\frac{\partial\theta_f}{\partial\xi} = 0 \quad \text{if} \quad u_\xi > 0 \quad \text{at}\, \xi = \xi_\infty$$

and then solving for different finite values of (x_∞, y_∞) $(= \frac{1}{2}\sinh\xi_\infty, \frac{1}{2}\cosh\xi_\infty)$, where $x_\infty = 11.6$, 23.2, 29.0, $y_\infty = 11.6$, 23.2, 29.0. The discretized equations were solved using a Gauss–Seidel iteration procedure in the following manner. Equation (16) was iterated to convergence and provided boundary conditions for equations (86) and (87); these were looped once in order to provide temporary values of ω which were used to solve equation (85) to convergence. Thence, $(\theta_s)_{ij}$ and ω_{ij} were updated, and the looping procedure was continued until the convergence criterion

$$\frac{\Sigma_i^{M_\xi}\Sigma_j^{M_\eta}|F_{ij}^{(n+1)} - F_{ij}^{(n)}|}{\Sigma_i^{M_\xi}\Sigma_j^{M_\eta}|F_{ij}^{(n+1)}|} < 10^{-6},$$

was satisfied; here, the superscript n denotes the iteration order within the (θ_f, ω) loop and F denotes the functions ω and θ_f. (The same condition was used for convergence within the iteration loops for ψ and θ_s, although for the latter M_ξ and M_η are replaced by M_x and M_y.) θ_f now provides updated boundary conditions for equation (16), which is again solved to convergence. Looping again for the fluid variables produces ψ_{ij} which in general differs from that obtained at the convergence of the previous (θ_f, ω) loop, and therefore the global convergence criterion was taken to be

$$\frac{\Sigma_i^{M_\xi}\Sigma_j^{M_\eta}|\psi_{ij}^{(\hat{n}+1)} - \psi_{ij}^{(\hat{n})}|}{\Sigma_i^{M_\xi}\Sigma_j^{M_\eta}|\psi_{ij}^{(\hat{n}+1)}|} < 10^{-6}$$

with $\hat{n}$ denoting the iteration order; effectively, $\hat{n}$ denotes the number of times that the conjugate condition (90) has been updated. In all cases, underrelaxation was used for equations (86) and (87) (relaxation parameters 0.7 and 0.1, respectively), overrelaxation, with parameter 1.8, for equation (85), and regular Gauss–Seidel for equation (16).

Several means were used to validate the code, in addition to comparison with the boundary-layer solution for high Rayleigh number to be described later. First of all, in Table 1, we show the effect of ξ_∞ on the mean Nusselt number, $\bar{Nu}$, for a 31×40 mesh when $k = 10^3$, $\lambda = 1$; the differences in $\bar{Nu}$ for the upper values of ξ_∞ are at most of the order of 2%. In addition, Fig. 3 shows the vertical velocity scaled with $Ra^{1/2}$ at $\eta = \pi/2$ (corresponding to $y = 0$), that is $u_\eta(\pi/2, \xi)/Ra^{1/2}$, when $k = 10^3$, $Ra = 10^2, 10^6$, $Pr = 1$, $x_\infty = 23.2$, using a 31×40 and 31×80 mesh; the (a) plot shows the velocity for $0 \leqslant x \leqslant x_\infty$, whilst the (b) plot is an enlargement of the (a) plot in the vicinity of $x = 0$. The plots show the velocity to be independent of grid size for this value of x_∞, as one would desire, and this was the value adopted for subsequent com-

Table 1. Effect of x_∞ on $\bar{Nu}$

Ra	Pr	x_∞	$\bar{Nu}$
10^2	1	11.6	2.406
		23.2	2.470
		29.0	2.490
10^6	1	11.6	18.654
		23.2	19.480
		29.0	19.774
10^2	10^3	11.6	2.660
		23.2	2.731
		29.0	2.759
10^6	10^3	11.6	25.270
		23.2	27.277
		29.0	27.980

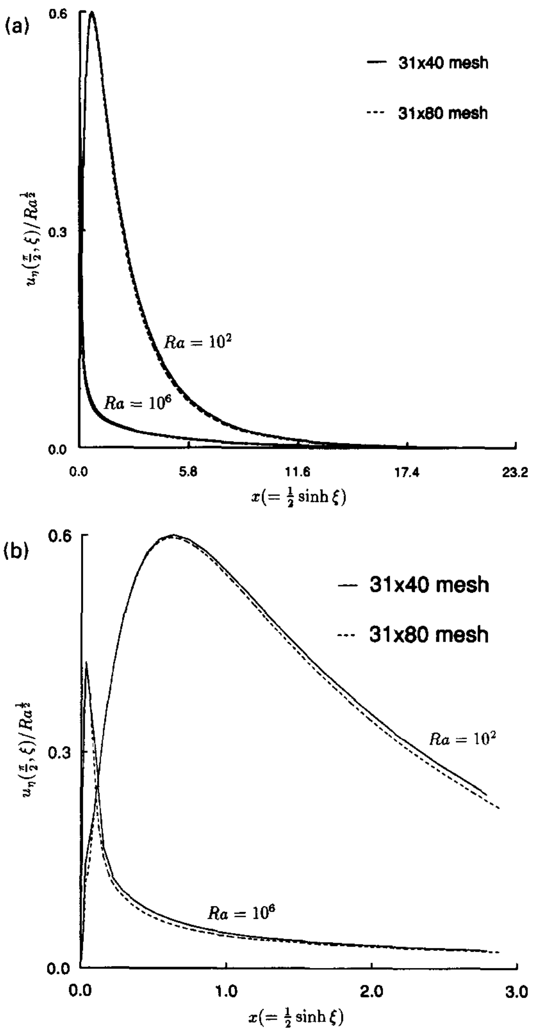

Fig. 3. (a) Scaled vertical velocity at $y = 0$ $(u_\eta(\pi/2, \xi)/Ra^{1/2})$ for 31×40 and 31×80 meshes for $Ra = 10^2$ and 10^6, $Pr = 1$, $k = 10^3$, $\lambda = 1$; (b) enlargement of (a) near $x = 0$.

putations. Furthermore, the (b) plot indicates that the meshes are sufficiently refined in the vicinity of $x = 0$ to resolve adequately the boundary layer there for $Ra = 10^6$. Further computations for $Pr = 10^3$ indicated the same trend, although we do not present the graphs here. The effect of grid size is demonstrated in Table 2, in which comparison is drawn with the mean Nusselt number for the leading unit length of an isothermal plate, using the result of Lefevre [12]. From Table 2, it is clear that the effect of grid size in ξ is greater than that in η; the difference between using 31 and 51 mesh points in η is less than about 2%, and therefore the lower value was used for later computations. More serious is the fact that even with 80 points in the ξ-direction, the error in $\bar{Nu}/Ra^{1/4}$ still appears to be around 4–5%. This is due to several factors: the fact that the conjugate boundary is not completely isothermal, nor of infinite length, as is the case for the analytical result with which comparison is being made. In view of these, and that the local Nusselt number is integrably singular at the leading edge for the high Rayleigh number case, as discussed in Section 3, the results indicate that the use of a 31×80 mesh incurs errors which are no greater than about 5% with respect to the mean Nusselt number, and certainly much less than this with respect to the velocity field.

5. RESULTS

Solutions to the full equations were computed for $\lambda = 0.1$, 1, $1 \leqslant k \leqslant 100$, $0.1 \leqslant Pr = 10^3$, $10^2 \leqslant Ra < 10^6$, using a 31×80 mesh.

First, streamline and isotherm behaviour for $\lambda = 1$, $Pr = 1$, are shown in Figs. 4–7; in each case, the (a) plot represents the streamfunction, the (b) plot the temperature. A comparison of Figs. 4b and 5b indicates that although for this value of Ra heat flow in the fluid is almost conductive, the lower value of k ensures a much larger temperature drop across the solid plate. Figures 6b and 7b also exhibit this sharp dependency on k, although this time the temperature drop is so great across the conducting plate for $k = 1$ that the conjugate boundary is almost at the ambient fluid temperature anyway. Thus the contour spacing of $\Delta\theta = 0.1$ picks out the thermal boundary layer in Fig. 6b, but is too large to pick it out in Fig. 7b. As for the (a) plots, Figs. 4 and 5 indicate relatively mild entrainment, which is not much affected by the difference in k for $Ra = 10^2$; Figs. 6 and 7 indicate a boundary-layer flow as one would expect, which is much more vigorous for $k = 100$ than for $k = 1$, as evidenced by the much closer contour spacings.

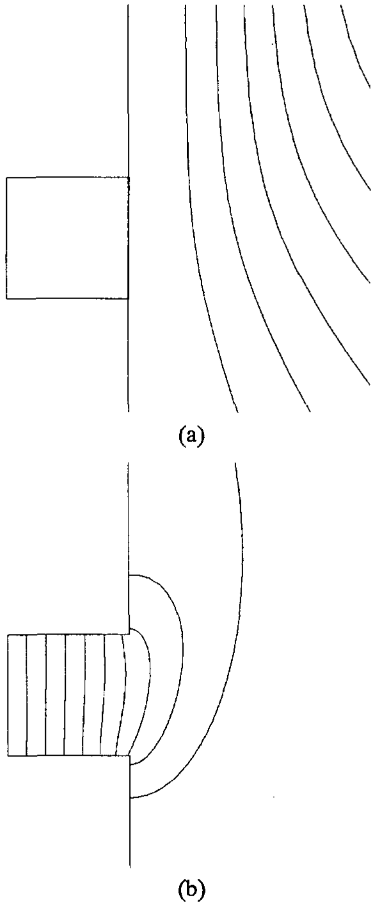

Fig. 4. Streamlines and isotherms for $k = 1$, $\lambda = 1$, $Pr = 1$, $Ra = 10^2$ ($\Delta\psi = 1$, $\Delta\theta = 0.1$).

Table 2. Comparison of $\bar{Nu}/Ra^{1/4}$ for computed solutions with analytical result for $Ra = 10^6(x_\infty = 23.2)$

	$\bar{Nu}/Ra^{1/4}$			
Pr	51×40	31×40	31×80	analytical
1	0.604	0.616	0.560	0.535
10^3	0.851	0.863	0.700	0.665

Figures 8–11 indicate the conjugate boundary temperature, the (a) plots, and the local Nusselt number, the (b) plots, for $Ra = 10^2$, 10^4, 10^6 for four sets of parameter values of Pr, k and λ. Where available, comparison is provided between the full numerical solutions and the coupled conduction-boundary layer formulation of Section 3.1; the only cases this has not been possible were for $Ra = 10^4$, $Ra = 10^6$ in Fig. 8, which correspond to a value of σ in excess of 1.6, as discussed in Section 3.2. Several obvious common features emerge from these plots. In general, θ_b obtained using the boundary-layer theory tends to be higher than that obtained by the full numerical solutions; this trend is in line with the results of Miyamoto *et al.* [6], albeit that their boundary-layer results were obtained using a different method. Nu, on the other hand, tends to be lower. Agreement between the two improves as Ra is increased, in line with expectation. The biggest discrepancy, even at $Ra = 10^6$,

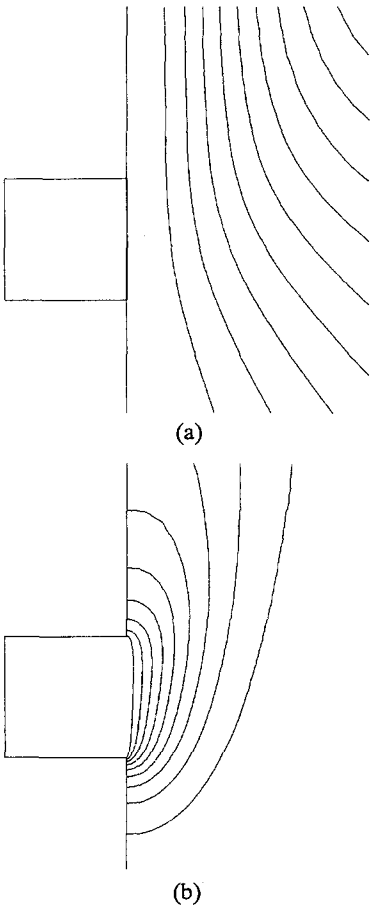
(a)

(b)

Fig. 5. Streamlines and isotherms for $k = 100$, $\lambda = 1$, $Pr = 1$, $Ra = 10^2$ ($\Delta\psi = 1$, $\Delta\theta = 0.1$).

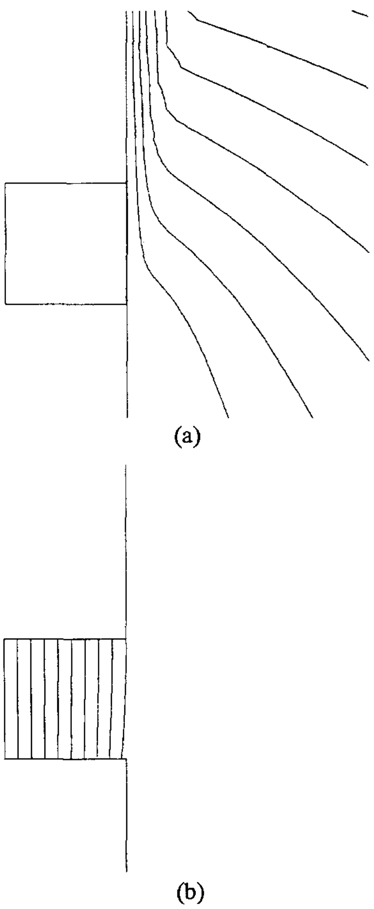
(a)

(b)

Fig. 6. Streamlines and isotherms for $k = 1$, $\lambda = 1$, $Pr = 1$, $Ra = 10^6$ ($\Delta\psi = 10$, $\Delta\theta = 0.1$).

arises at the leading and trailing edges of the plate. The coupled conduction–boundary layer formulation, which takes account of the singularity in Nusselt number at the leading edge, produces a value of θ_0 a few percent higher than the computed solution. For high but finite Rayleigh numbers, at the heart of this discrepancy lies the fact that the velocity for the fully computed solution at the leading edge is non-zero, whereas we have assumed that the velocity there is zero for the boundary-layer method. However, we note that as *Ra* is increased, agreement for θ_0 is seen to improve as one would expect on physical grounds: namely, as *Ra* is increased, there is less and less transfer of heat upstream to generate the buoyancy force that would be necessary to cause non-stagnant flow there. Consequently, the assumption that the upstream flow is stagnant improves with increasing *Ra*. At the trailing edge, the elliptic nature of the equations for the full computations ensures that the temperature decreases slightly in view of the discontinuity in the boundary condition for θ_f for $y > \frac{1}{2}$. Furthermore, there is a singularity in the Nusselt number here also, a feature which the boundary-layer theory cannot pick out. The trailing edge features, whilst quite marked for all the plots as regards *Nu*, are less severe for θ_b for the larger aspect ratio plate in Figs. 8a and 9a.

In general, θ_b is monotonic increasing and *Nu* monotonic decreasing with y, except in the trailing edge region just mentioned. The increase in θ_b with y is closest to linear in Figs. 8a and 9a for $\lambda = 1$, less so in Figs. 10a and 11a for $\lambda = 0.1$. Furthermore, in the former, the difference in maximum and minimum temperatures at the conjugate boundary differs by less than 0.1, but is as high as 0.2 for the aspect ratio 0.1 plate. Comparison between Figs. 8a and 10a demonstrates the role of the aspect ratio in effectively controlling plate conductivity, with a lower value of λ having the same effect as the increase in k in Fig. 9a. Comparison of Figs. 10a and 11a shows that an order of magnitude decrease in *Pr* causes a slight increase in θ_b which becomes more pronounced as *Ra* increases; however, the scale of the change is much less than is generally due to order of magnitude increases in any one of *Ra*, k or λ.

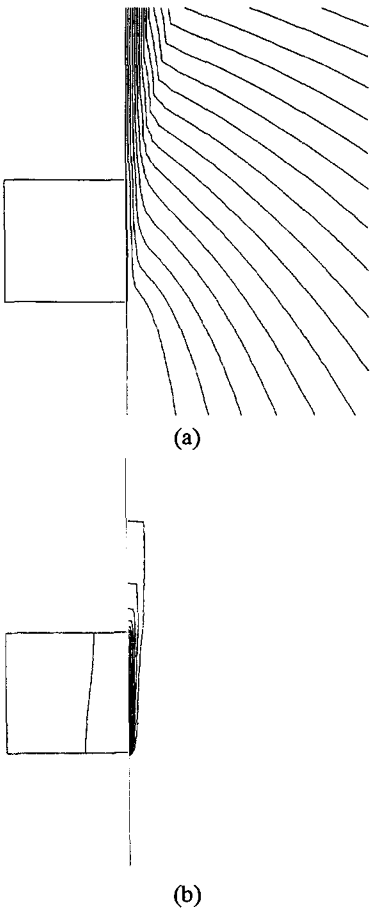

Fig. 7. Streamlines and isotherms for $k = 100$, $\lambda = 1$, $Pr = 1$, $Ra = 10^6$ ($\Delta\psi = 10$, $\Delta\theta = 0.1$).

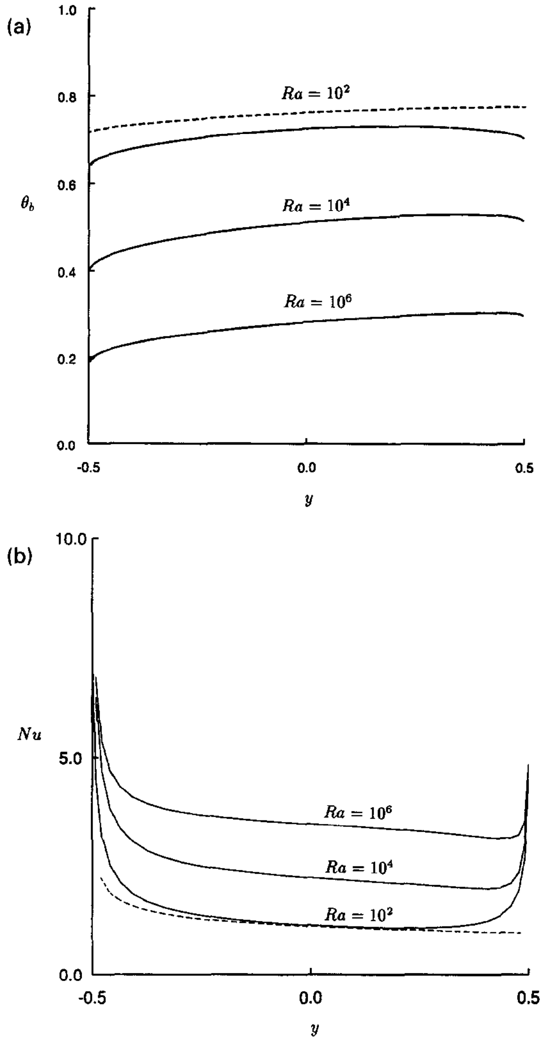

Fig. 8. (a) Boundary temperature (θ_b) and (b) local Nusselt number (Nu) vs distance along plate (y) for $Ra = 10^2$, 10^4, 10^6, $Pr = 1$, $k = 5$, $\lambda = 1$ (dashed lines represent boundary-layer solutions, solid lines represent full numerical solutions).

Overall, these comparisons indicate that the parameter λ is most responsible for determining the local profile of θ_b and Nu at the conjugate boundary, as well as the averaged values of θ_b and Nu at the boundary. Ra, Pr and k, on the other hand, appear to be influential mainly in determining only the averaged values, all the more so for lower values of Ra. In particular, the relatively small deviation from the mean value of the profile of $\theta_b(y)$ for $\lambda = 1$ suggests that, in this case, the averaged approach of Section 3.3 should be able to provide good estimates for $\bar{\theta}_b$ and $\bar{Nu}$. This is demonstrated in Figs. 12 and 13 for $Pr = 0.1$, 100, $k = 1$, 2.5, 10. In the (a) plots, the analytical values for $\bar{\theta}_b$ were obtained using equation (74); the analytical values for $\bar{Nu}$ were obtained by using equation (84) for $Pr = 0.1$, and equation (77) for $Pr = 100$. In all cases, as one would expect, agreement with the full numerical computations is better for $Ra = 10^6$ than for $Ra = 10^2$, although even for the latter case, agreement appears to be sufficiently good for the formulae to be able to be used reliably for a wide range of Rayleigh number.

6. CONCLUSION

Conjugate free convection due to a vertical plate adjacent to a semi-infinite fluid region has been analysed theoretically. In addition to numerical solutions to the full governing equations for a wide range of the four relevant nondimensional parameters (Ra, Pr, k, λ), the problem was reformulated for the high Rayleigh number regime by coupling conduction in the solid with the free convective boundary-layer flow at the conjugate boundary. In the resulting equations, the number of dimensionless parameters is reduced to three, following the emergence of $Ra^{1/4}/k$ as just one parameter. These equations were solved using an iterative scheme involving a standard bound-

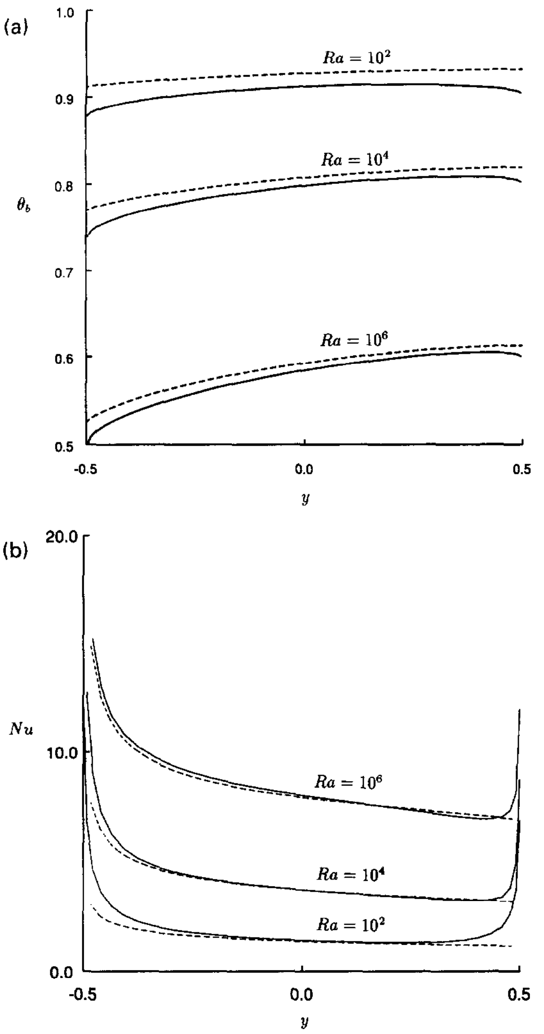

Fig. 9. (a) Boundary temperature (θ_b) and (b) local Nusselt number (Nu) vs distance along plate (y) for $Ra = 10^2$, 10^4, 10^6, $Pr = 1$, $k = 20$, $\lambda = 1$ (dashed lines represent boundary-layer solutions, solid lines represent full numerical solutions).

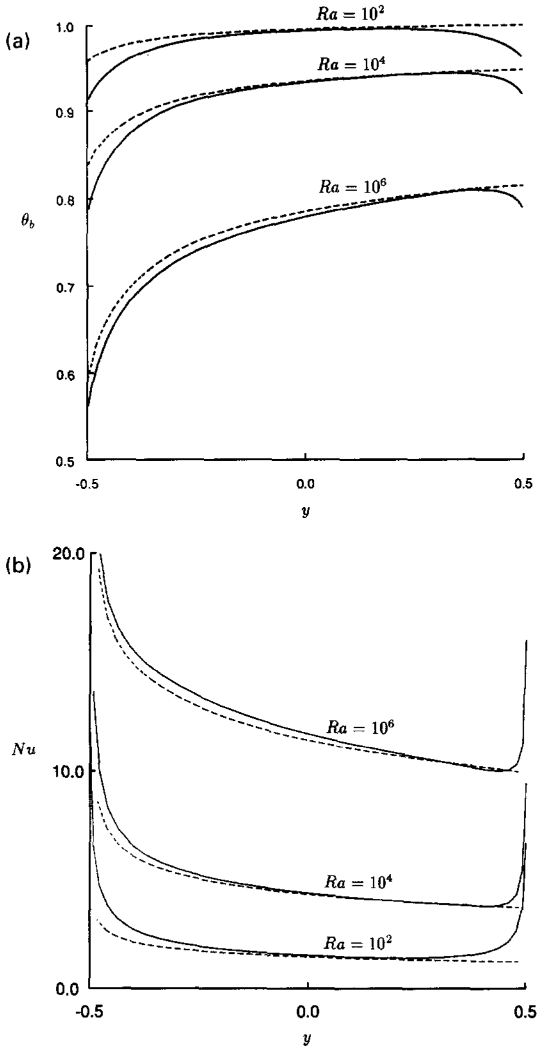

Fig. 10. (a) Boundary temperature (θ_b) and (b) local Nusselt number (Nu) vs distance along plate (y) for $Ra = 10^2$, 10^4, 10^6, $Pr = 1$, $k = 5$, $\lambda = 0.1$ (dashed lines represent boundary-layer solutions, solid lines represent full numerical solutions).

ary-layer solver and Gauss–Seidel iteration for the solid. The solutions showed good agreement with the full computations, as did the results of an alternative formulation designed to provide a quick and economic alternative for determining the average conjugate boundary temperature and Nusselt number in engineering calculations.

The main purpose of this work was to include the effects of finite aspect ratio of the heating plate, thereby superceding earlier work for thin plates. It was found that for larger aspect ratios, the deviation in the temperature at the fluid/solid interface from the average was not as large as that for smaller ones, although this trend was less evident at lower Rayleigh numbers. Furthermore, leading and trailing edge effects were observed to be responsible for discrepancies between the methods of solution. Boundary-layer theory indicates a higher temperature at the leading edge than the full computations; at the trailing edge, on the other hand, the full computations indicate a temperature drop in the face of the oncoming change in thermal boundary conditions. Furthermore, the trailing edge temperature drop is more evident for lower aspect ratios than for higher ones, all the more so for higher values of Ra. In all cases, in addition to the expected $(y+\frac{1}{2})^{-1/4}$ singularity in Nu at the leading edge, the full computations indicate a singularity in Nu at the trailing edge also. However, the good agreement with the averaged theory for $\bar{Nu}$, which takes account only of the first singularity, suggests that the contribution of

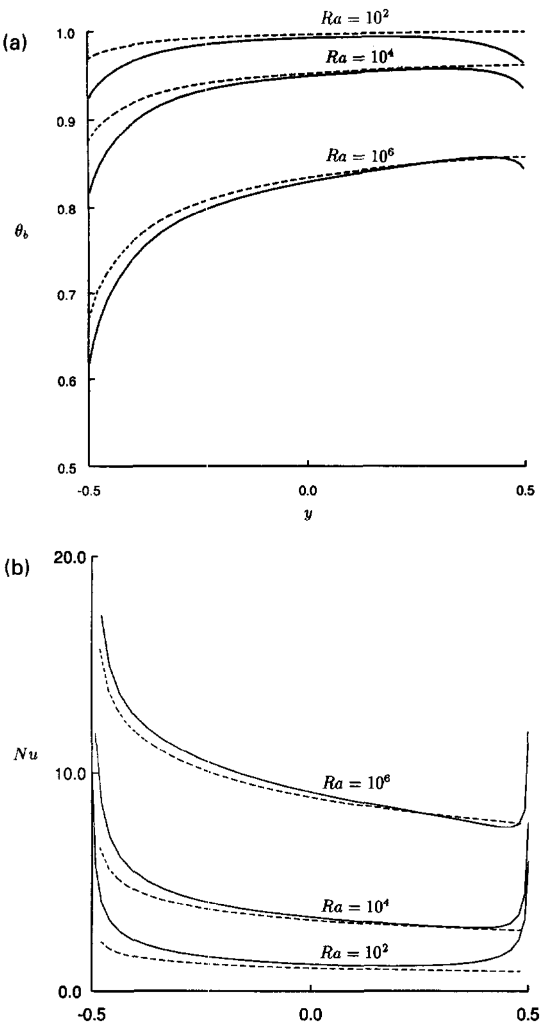

Fig. 11. (a) Boundary temperature (θ_b) and (b) local Nusselt number (Nu) vs distance along plate (y) for $Ra = 10^2$, 10^4, 10^6, $Pr = 0.1$, $k = 5$, $\lambda = 0.1$ (dashed lines represent boundary-layer solutions, solid lines represent full numerical solutions).

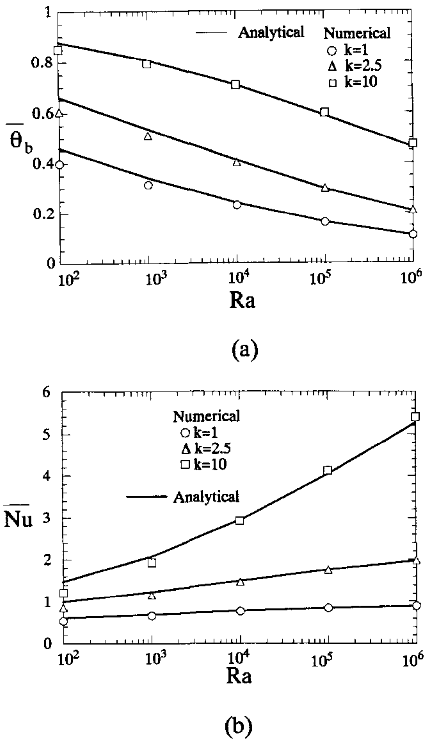

Fig. 12. (a) Average boundary temperature ($\bar{\theta}_b$) and (b) average Nusselt number ($\bar{Nu}$) vs Rayleigh number (Ra) for $k = 1, 2.5$ and 10 ($\lambda = 1$, $Pr = 0.1$).

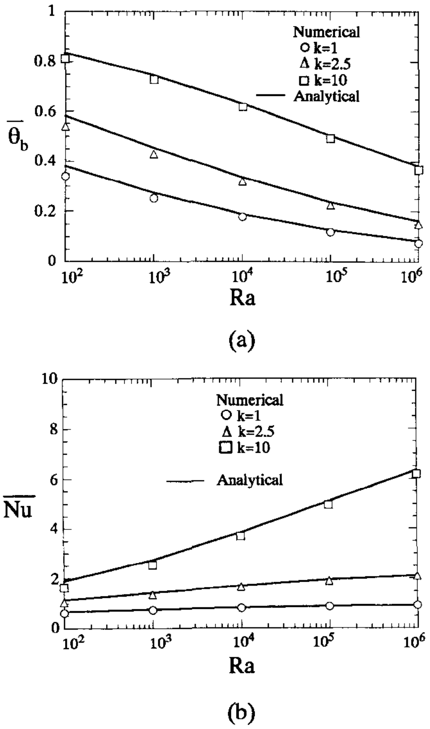

Fig. 13. (a) Average boundary temperature ($\bar{\theta}_b$) and (b) average Nusselt number ($\bar{Nu}$) vs Rayleigh number (Ra) for $k = 1, 2.5$ and 10 ($\lambda = 1$, $Pr = 100$).

this intense local heating to the overall heat transfer to the fluid is comparatively small. Finally, it is worth noting that the boundary-layer approach we have adopted here appears to be free of the problems involving the leading edge encountered by Miyamoto *et al.* [6], since the singular contribution to the Nusselt number may be resolved using analytical techniques.

REFERENCES

1. S. W. Hong, Natural circulation in horizontal pipes, *Int. J. Heat Mass Transfer* **20,** 685–691 (1977).
2. M. D. Kelleher and K. T. Yang, A steady conjugate heat transfer problem with conduction and free convection, *Appl. Sci. Res.* **17,** 240–268 (1967).
3. A. E. Ziness, The coupling of conduction with laminar convection from a vertical plate with arbitrary surface heating, *J. Heat Transfer*, **92,** 528–535 (1970).
4. K. Chida and Y. Katto, Study on conjugate heat transfer by vectorial dimensional analysis, *Int. J. Heat Mass Transfer* **10,** 453–460 (1976).
5. L. B. Gdalevich and V. E. Fertman, Conjugate problems of natural convection, *Inzh-Fiz. Zh.* **33,** 539–547 (1977).
6. M. Miyamoto, J. Sumikawa, T. Akiyoshi and T. Nakamura, Effects of axial heat conduction in a vertical flat plate on free convection heat transfer, *Int. J. Heat Mass Transfer* **23,** 1545–1553 (1980).
7. M. Miyamoto and S. Nishiyama, Numerical solutions of unsteady laminar free convection on a semi-infinite vertical plate (in Japanese), *Mem. Fac. Engng Yamaguchi Univ.* **28,** 105–114 (1976).
8. M. Miyamoto and J. Sumikawa, Effect of wall conduction on a laminar free convection heat transfer, *Proceedings of 15th Annual Symposium, Heat Transfer Society of Japan*, pp. 217–219 (in Japanese) (1978).
9. J. Timma and J.-P. Padet, Etude théorique du couplage convection-conduction en convection libre laminaire sur une plaque plane verticale, *Int. J. Heat Mass Transfer* **28,** 1097–1104 (1985).
10. A. Pozzi and M. Lupo, The coupling of conduction with laminar natural convection along a flat plate, *Int. J. Heat Mass Transfer* **31,** 1807–1814 (1985).
11. J. H. Merkin and I. Pop, Conjugate free convection on a vertical surface (submitted).
12. E. J. Lefevre, Laminar free convection from a vertical plane surface, *Ninth International Congress of Applied Mechanics*, Brussels, Paper 1–168 (1956).
13. S. V. Patankar, *Numerical Heat Transfer and Fluid Flow*. Hemisphere, Washington, DC (1980).
14. T. Cebeci and P. Bradshaw, *Physical and Computational Aspects of Convective Heat Transfer*. Springer, Berlin (1984).
15. J. P. Holman, *Heat Transfer* (4th Edn.). McGraw-Hill, New York (1976).